Atmospheric rivers over the Bay of Bengal lead to northern Indian extreme rainfall

Article

Accepted Version

Yan, Y., Zhao, T., Ni, G. and Sun, T. (2018) Atmospheric rivers over the Bay of Bengal lead to northern Indian extreme rainfall. International Journal of Climatology, 38 (2). pp. 1010-1021. ISSN 0899-8418 doi: https://doi.org/10.1002/joc.5229 Available at https://centaur.reading.ac.uk/71998/

INTERNATIONAL JOURNAL OF CLIMATOLOGY
RMetS Royal Meteorological Society

Atmospheric Rivers over the Bay of Bengal Lead to Northern Indian Extreme Rainfall

Journal:	*International Journal of Climatology*
Manuscript ID	JOC-16-0920.R2
Wiley - Manuscript type:	Research Article
Date Submitted by the Author:	08-Jul-2017
Complete List of Authors:	Yang, Yan; Tsinghua University, State Key Laboratory of Hydro-Science and Engineering, Department of Hydraulic Engineering Zhao, Tongtiegang; Commonwealth Scientific and Industrial Research Organization, Division of Land and Water NI, Dr. Guangheng; Tsinghua university. State Key Laboratory of Hydro-Science and Engineering, Department of Hydraulic Engineering Sun, Ting; Tsinghua University, State Key Laboratory of Hydro-Science and Engineering, Department of Hydraulic Engineering
Keywords:	Atmospheric river, Bay of Bengal, Tropical cyclone, Extreme rainfall, ERA-Interim dataset
Country Keywords:	Bangladesh, India

Atmospheric Rivers over the Bay of Bengal Lead to Northern Indian Extreme Rainfall

Yan Yang[1], Tongtiegang Zhao[3], Guangheng Ni[1], Ting Sun[1,2*]

1) State Key Laboratory of Hydro-Science and Engineering, Department of Hydraulic Engineering, Tsinghua University, Beijing 100084, China

2) Department of Meteorology, University of Reading, Reading, RG6 6BB, UK

3) Commonwealth Scientific and Industrial Research Organization, Division of Land and Water, Melbourne 3168, Australia

* Corresponding Author: sunting@tsinghua.edu.cn

Abstract

Atmospheric rivers (ARs), filamentary patterns of strong water vapor fluxes, play a prominent role in global poleward moisture transport and have profound impacts on extreme rainfalls (ERs). Previous AR research has mainly focused on the mid-latitude regions, whereas the characteristics of ARs in low latitudes and their relationship with local ERs remain largely unknown. This study investigates the spatiotemporal characteristics of ARs over the Bay of Bengal and their relationship with ERs after landing on the northern Indian subcontinent using the ERA-Interim reanalysis data. During the study period from 1979 to 2011, a total of 149 ARs have been identified, which feature a bimodal temporal pattern with more events observed in May and October. The AR axes generally stretch northeastwards over the bay and land in Bangladesh and Burma. 24% of ARs occurring during tropical cyclones implies a possible connection between them, in addition to the similar intra-annual distribution. In summer, as the tropical cyclones are weak and the northward water vapor flux decreases due to topographic blocking of the Western Ghats, it is less likely to form intensified water vapor pathway, though the atmospheric humidity is high in the study region. Furthermore, a close correlation between ARs and ERs is manifested. A large proportion of ARs would lead to ERs, with a small fraction of ERs occur after ARs. In addition, although persistent ARs constitute the majority of identified events, rainfall intensity will not be enhanced by the increase in AR duration. This study enriches the knowledge of AR characteristics in low latitudes and provides new pathways to understand the

hydrological cycles in the Indian Peninsula and the Bay of Bengal.

Keywords:

Atmospheric river; Bay of Bengal; Tropical cyclone; Extreme rainfall; ERA-Interim dataset

1. Introduction

Atmospheric rivers (ARs), featured by long, narrow corridors of enhanced water vapor transport, are responsible for more than 90% of the horizontal water vapor transport from tropics or subtropics into higher latitudes, and facilitate the precipitation that is crucial to water supply (Zhu and Newell 1998; Ralph et al. 2011a; Bao et al. 2006). Some strong ARs that contain large amount of water vapor associated with fierce winds may lead to extreme rainfall (ER) and floods (e.g., Ralph et al. 2004; Lavers et al. 2011). Consequently, ARs are widely recognized for the crucial role in the global water cycle (e.g., Zhu and Newell 1998) and particularly those hydrometeorological extremes (Neiman et al. 2008b).

In the mid-latitudes, these intensified water vapor plumes are often manifested as moisture convergence in extratropical cyclone warm sectors and the pre-cold-frontal low-level jet region (Ralph et al. 2004, 2006; Bao et al. 2006; Stohl et al. 2008). Two moisture sources are considered responsible for AR formation: local moisture convergence along the trailing cold fronts and direct poleward transport of tropical moisture (Bao et al. 2006). In addition, Dacre et al. (2015) found that water vapor in the cyclones' warm sector is more responsible for the generation of high water vapor content, compared with long-distance transport of water vapor from subtropics, which explains the high frequency of wintertime ARs in mid-latitudes. Furthermore, Zhu and Newell (1998) speculated that tropical ARs may be related to large-scale convergence in

66 boundary regions such as the intertropical convergence zone (ITCZ), rather than
67 baroclinic cyclones.
68
69 In the vicinity of ARs, cloud-top temperatures are colder, indicating that deeper clouds
70 (mid- and high clouds) are associated with deep convective systems that promote heavy
71 precipitation by strong upward motion up to the tropopause with a large amount of
72 cloud liquid (Ralph et al. 2004, 2011b). Most of the water vapor in ARs is transported
73 within the lowest 2.5 km of the atmosphere with moist-neutral stratification (Ralph et al.
74 2005). The combination of lower-troposphere moist neutrality and strong horizontal
75 winds creates an ideal avenue for strong orographic precipitation when ARs approach
76 high terrains (Ralph et al. 2011a; Lavers et al. 2011, 2012; Viale and Nunez 2010). For
77 example, ARs stretching from the eastern Pacific Ocean to western North America are
78 regarded as a primary meteorological contributor in flood generation and water
79 resources in California as ARs bring in 20-50% of the total precipitation in the long
80 term (Dettinger et al. 2011). Additionally, landfalling AR is found to be a strong
81 precursor to the ER in the western European seaboard: 8 of the 10 largest ER events
82 were preceded by ARs (Lavers and Villarini 2013b). The concept of ARs provides a new
83 and objective framework to examine and quantify atmospheric conditions related to ERs
84 (Ralph et al. 2006).
85
86 Previous techniques for AR identification are primarily based on the intensity and

spatial features of atmospheric water vapor (Gimeno et al. 2014). The intensity is usually quantified by the vertically integrated water vapor (IWV) and vertically integrated horizontal water vapor transport (IVT). IWV can either be retrieved from the Special Sensor Microwave Imager (SSM/I) (Ralph et al. 2004), or calculated using atmospheric reanalysis data; while IVT can be determined by using atmospheric reanalysis data (Zhu and Newell 1998). Compared with IWV, IVT is more desirable for AR detection due to its closer relationship with orographic precipitation (Neiman et al. 2002; Guan and Waliser 2015). In terms of geometric features, length, width and length/width ratio are usually used in AR identification (Guan and Waliser 2015). However, thresholds of these measures are not universal but determined region by region (Gimeno et al. 2014). For instance, Neiman et al. (2008a) suggested that narrow plumes of SSM/I with IWV values >20 mm (i.e., >2000 km long and <1000 km wide) can be identified as ARs along the west coast of North America, whereas ARs at the Midwestern USA are found to have higher IWV intensity (in the range of 30–55 mm) and longer extension (about 3000 km) (Moore et al. 2012).

Although ARs in mid-latitudes are well studied by previous research, characteristics of ARs in lower latitudes are remaining largely unknown. Meanwhile, the Bay of Bengal is under strong influence of Indian monsoon, South Asian monsoon and notable tropical cyclones and thus becomes vulnerable to devastating rainfall and floods that can be induced by ARs. Additionally, inland penetration of ARs in concomitant with the

Himalayas may facilitate the topographic ERs in this region. As such, we focus on ARs over the Bay of Bengal and examine their relationship with ERs over the Indian subcontinent (Figure 1).

The objectives of the study are (1) to investigate the spatiotemporal characteristics of ARs over the Bay of Bengal, and (2) to examine their relationship with ERs in the northern Indian subcontinent. In the remainder of this paper, we first introduce an algorithm for AR identification and apply it over the Bay of Bengal. Next, based on the results of identified ARs, we analyze their characteristics and relationship with ERs in the northern Indian subcontinent.

2. Methodology

2.1 Data

The ERA-Interim dataset (Dee et al. 2011) at a 1.5° resolution spanning from 1979 to 2011 is used in this study. The ERA-Interim dataset features better representation of hydrological cycle (Berrisford et al. 2011) and has been widely used in identifying moisture origins (Zhao et al. 2015), delineating water vapor transport pathways (Dong et al. 2016), etc. Especially, it can represent key AR characteristics (Guan and Waliser 2015). In the dataset, the specific humidity and the zonal and meridional wind fields are available at a 6 h resolution, while the precipitation and evaporation are provided at a 3 h resolution. The specific humidity and horizontal wind fields are used in the AR

identification algorithm, while evaporation between 1000 hPa and 175 hPa is used to correct precipitation by taking condensation as a part of precipitation. Also, as the rainfall is available at a relative coarse spatial resolution (i.e., 1.5°), some subsynoptic-scale gradients, such as those associated with orographic processes over mountain barriers, may be smoothed out (Rutz et al. 2014). Nevertheless, the ERA-Interim precipitation has the same spatial coverage and consistency between the AR and ER results that will facilitate the exploration of their correlation in the later sections.

2.2 ER Identification

An ER is defined as the 90th percentile of the maximum daily rainfall over the study area during 1979-2011 (Champion et al. 2015). In addition, only rainy days with daily precipitation larger than 1 mm are included (Eiras-Barca et al. 2016). The 90th percentile threshold is calculated separately for each month (Figure 2).

2.3 AR Identification

We modify the method in Lavers and Villarini (2013a) for central United States in two aspects: (1) Two reference latitudes are used in this study: 24°N and 27°N that represent the coastal and interior areas respectively, in consideration of the variation of IVT strength along latitude; (2) Equivalent width and direction thresholds are used in the back trajectory algorithm in order to filter out invalid identification results.

The detection method is based on the IVT field derived from specific humidity and wind fields between 1000 and 300 hPa given by

$$\mathrm{IVT} = \sqrt{\left(\frac{1}{g}\int_{1000}^{300} qudp\right)^2 + \left(\frac{1}{g}\int_{1000}^{300} qvdp\right)^2} \quad (1)$$

where q is the specific humidity in kg kg^{-1}, u and v are the zonal wind and meridional wind in m s^{-1}, respectively, g is the acceleration of gravity in m s^{-1} (Neiman et al. 2008a; Lavers and Villarini 2013a, 2013b).

Monthly IVT strength thresholds are applied in the AR identification considering the notable intra-annual variability of IVT intensity (Champion et al. 2015) and ER occurrence. The IVT threshold is determined as follows. The maximum values of IVT at reference latitudes (i.e., 24°N and 27°N) at 1200 UTC of each day are first regrouped by month, then the 85th percentiles of each group are determined as the monthly thresholds. We note that IVT results smaller than 250 kg m^{-1} s^{-1} are excluded as they are too small in winter (Rutz et al. 2014).

Besides the IVT strength threshold determination, the two reference latitudes are also used in locating the ending point of AR axis (i.e., the central line of an AR). By identifying ARs based on the three latitudes of the study area (i.e., 24 °N, 25.5 °N and 27 °N), we found the results based on 24°N and 27°N are sufficient to cover all AR

events. Thus, we employ 24°N and 27°N as reference latitudes (Full details of reference latitude selection refer to Appendix).

The next step of AR identification is to determine the AR axis, which in combination with geometry thresholds will be used to filter out the objects with less physical meanings: as ARs refer to the strong poleward water vapor transport, objects not satisfying such directionality need to be excluded. To start with, we define the ending point of AR axis as the location of the maximum IVT at reference latitudes. Then a back trajectory algorithm is used in the axis identification (Figure 3): we search for the highest IVT by comparing the adjacent grid cells to the south, southeast and southwest, which are selected because of the poleward transport feature, and such procedure is iterated until a total of 14 successive grid points are obtained to form an axis. If 14 grids are taken south of reference latitude, the identified axis would be more than 2000 km long (Ralph et al. 2004).

Direction and width thresholds are then applied to distinguish ARs from monsoon and tropical cyclones. Moisture convergence in a low-pressure center and intense surface wind of summer monsoon are likely to be mistakenly identified as ARs if only IVT strength and length are considered. The direction of an AR should satisfy the condition that the included angle between mean transport direction and the line connecting two endpoints of the axis is not greater than 45°. The mean transport direction is the mean

moisture transport direction of grids along the axis. Here we use the equivalent width (EW) to represent the width of an AR, which should be less than 1000 km (7 grids) (Ralph et al. 2004; Neiman et al. 2008a). The EW is calculated as:

$$EW = \frac{area}{length} \quad (2)$$

where length is the number of the contiguous grids (14 in this case), area is the total number of grids with IVT strength greater than the monthly threshold in the axis coverage region, which is a sub-domain of the rectangular region extending diagonally from (76.5°E，0°N) to (99°E，30°N): if the axis stretches zonally (meridionally), its endpoints will determine the north-south (west-east) boundary of the coverage region.

To briefly summarize, AR identification includes three steps: (1) obtaining the original AR occurrence time based on the IVT strength threshold; (2) conducting AR axis identification and (3) filtering out the mistakenly identified AR structures with width and direction thresholds. Figure 4 illustrates the brief workflow of AR identification algorithm.

3. Results and discussion

3.1 IVT intensity

Apparent seasonality in the atmospheric water vapor indicated by IVT is observed in the study region (Figure 5). This pattern features high precipitation due to the strong influence of southwesterly monsoon with abundant water vapor (Zhao et al. 2015). In

general, high IVT ($\geq$ 250 kg m^{-1} s^{-1}) is observed in summer (JJA, Figure 5b) and autumn (SON, Figure 5c) but winter (DJF, Figure 5d) and spring (MAM, Figure 5a). Annual IVT exhibits a single-peak trend with the maximum in July as high as 600 kg m^{-1} s^{-1}. In May (not shown) and autumn (SON, Figure 5c), the water vapor belt forms over the bay and extends meridionally to the northeast of the study region. While in JJAS (Figure 5e), the seasonal movement of the ITCZ, manifesting as monsoon, prompts the seasonal rainfall variations. High rainfalls occur over the monsoon zone around 20° N stretching northwestward from the head of the Bay of Bengal. And most of the summertime monsoon rainfalls occur in association with the propagation of synoptic-scale convective systems from the Bay of Bengal along the monsoon zone (Gadgil 2003; Schneider et al. 2014). Also, as the East Asian monsoon becomes stronger in autumn, water vapor brought by the southwesterly and East Asian monsoon converges near the Longitudinal Range-Gorge Region in China (yellow box in Figure 5c). While the wintertime IVT is relatively too small to impose apparent influence on the precipitation.

Inland penetration of ARs implies their possible impacts on areas that are distant from the landfalling locations (Guan and Waliser 2015; Rutz et al. 2014). Considering the high possibility of AR penetration, it is necessary to examine the possible extents of ARs in the study region. As such, the dependence of IVT intensity on latitude is assessed using their monthly thresholds of each latitude (Figure 6). A slight increase in IVT is observed from 24°N to 25.5°N, which can be attributed to the high local

evaporation from densely covered rivers in this area. Although IVT then decreases from 25.5°N to 27°N, the southern foot of the Himalayas, its relatively high value (larger than 250 kg m^{-1} s^{-1}) implies ARs may penetrate into the interior area of the study region.

3.2 AR

The intra-annual distribution of AR demonstrates a clear dual-peak pattern (peaking in May and October) (Figure 6), which differs from single-peak pattern of ARs (peaking in winter) observed in mid-latitudes. It is also noteworthy that the intra-annual variation in AR does not follow that in IVT (single-peak pattern in summer), implying the summertime decrease in AR events is caused not by the reduced IVT intensity but possibly by the seasonal movement of water vapor belts: as the belt encounters the Western Ghats (cf. Section 3.1), the high deficit in water vapor hampers the formation of AR in summer.

To investigate the spatial pattern of ARs, AR axis is introduced as the indicator. Comparable spatial occurrence patterns of ARs are observed in spring (Figure 7a) and autumn (Figure 7c) with inland occurrence in Burma, Bangladesh and India. While less occurrence of ARs is observed in summer, the intensity of AR is much stronger than those in other seasons with deeper penetration (Figure 7b). The occurrence of AR is significantly less in winter (Figure 7d). Figure 8a-8d show examples of ARs identified in the four seasons.

Considering the similar bimodal temporal distribution of ARs and tropical cyclones over the Bay of Bengal (Li et al. 2012), we hypothesize that possible correlation may exist between them. Using the tropical cyclone best-track data from the Joint Typhoon Warning Center (JTWC), we compare the occurrence of ARs and tropical cyclones. The results indicate that 24% of ARs occurred during tropical cyclones with most in the end of the best track periods. We note that this percentage could be larger because ARs that occurred after the tropical cyclones were excluded. Compared with the findings in southeastern United States that only ~7% of ARs occurred during tropical and subtropical cyclones (Debbage et al. 2017), it is indicated that ARs in the Bay of Bengal are heavily influenced by tropical activity. Figure 8c shows the spatial pattern of a typical AR that occurred during the active tropical cyclone period, indicating the role of tropical cyclones in facilitating the longitudinal transport of water vapor that feeds ARs.

Based on the hypothesis, the low summertime occurrence of ARs may also be attributed to other factors (e.g., vertical wind shear and vorticity (Li et al. 2012)) that limit the formation of tropical cyclones, in addition to the weakened water vapor transport due to topographic blocking (cf. Section 3.1). Also, water vapor belts are sometimes led by the local convective systems to the East India during the summer monsoon (Figure 8e).

3.3 Relevance to Extreme Precipitation

The relevance of ARs to ERs is investigated by testing the following hypotheses: 1) ERs occur after ARs and 2) ARs lead to ERs. During the period from 1979 to 2011, a total of 1190 ERs have been identified with the spatial distribution concentrating mainly along the south foot of the Himalayas (Figure 9), suggesting the importance of orographic effect in the formation of ERs. Furthermore, we term those ERs that occur after ARs no later than 24 hours and appear in the vicinity of the AR axis (i.e. within 1.5 degree from the AR axis) as AR-related ERs (AERs) hereinafter. The above hypotheses are then tested through two ratios: 1) r_{ER} (the occurrences of AERs over all ERs) and 2) r_{AR} (the occurrences of AERs over all ARs). r_{ER} indicates the fraction of ERs that are associated with ARs, whereas r_{AR} suggests the fraction of ARs that lead to ERs.

Noticeable seasonality is found in r_{ER} (Figure 10a) with higher values of ~14% observed in October and November (the post-monsoon season) while the lowest values in summer and winter. Such seasonality could be explained by the variability of synoptic forcing and large-scale moisture availability (Eiras-Barca et al. 2016). During the transitional monsoon season, AERs are favored by the abundant moisture conveyed by ARs that satisfies the dynamic conditions for ERs. However, in the warm season, precipitation tends to be more associated with convective systems (Lavers and Villarini 2013b; Champion et al. 2015; Eiras-Barca et al. 2016; Gadgil, 2003). Hence, the moisture availability is no longer a restriction due to local moist convection favored by higher temperatures. Meanwhile the tropical cyclones are less frequent, so ERs are

mostly attributable to local convective systems rather than ARs (Champion et al. 2015).

Apparent seasonality is found in r_{AR} as well (Figure 10b): wintertime values are much higher than those in other seasons. Compared with r_{ER}, r_{AR} shows larger magnitude over the whole year, indicating stronger correlation of AER with AR than with ER. In particular, during the dry boreal winter, the high r_{AR} (i.e., >50%) highlights the crucial role of ARs in forming ERs by supplying abundant moisture. As for the spatial distribution of ERs, local topographic lift is found of great importance in facilitating AERs. Therefore, higher winter half-year r_{AR} also indicates the potential of ARs in inland penetration. On the other hand, the relatively low r_{AR} in spring could be attributed to ARs that are not strong enough to penetrate deeply inland.

Based on the results of r_{ER} and r_{AR}, we thus infer that only a very small fraction of ERs occur after ARs whereas a high portion of ARs can lead to ERs in the study region. Furthermore, as the positive relationship is found between the duration of AR and the rainfall/streamflow during AER (i.e. longer AR duration potentially induce higher rainfall/streamflow, see Lavers and Villarini 2013a in central United States, Ralph et al. 2006 in northern California), we also examine such relationship in the study region.

ARs are categorized into three groups according to their durations: 1) AR-all: all AR events are included; 2) AR-12h: AR events longer than 12 hours are included; 3)

316 AR-18h: AR events longer than 18 hours are included. Results show that 70% of the
317 149 AR events last more than 12 hours, and up to 50% ARs fall into group AR-18h. It is
318 noteworthy that similar r_{AR} values of ~50% are found across the three groups (Figure
319 11), suggesting the AR duration has minimal influence on the intensity of ERs.
320

321 **4. Concluding remarks**

322 In this study, we investigate the spatiotemporal characteristics of ARs over the Bay of
323 Bengal and their correlation with ERs in study area. In total, 149 ARs are identified
324 from 1979 to 2011 using a modified algorithm of AR identification in the IVT field,
325 over 50% of which last more than 18 hours. The modification includes width and
326 direction thresholds, in addition to length and IVT strength criteria, to filter out the
327 monsoon and tropical cyclones, which could be mistakenly identified as ARs in the
328 tropics. The choice of reference latitude is shown to be crucial in AR identification,
329 given the remarkable variation of IVT threshold along latitude. Two reference latitudes
330 are found to be sufficient to capture all AR events of the study region.
331

332 The intra-annual variation of AR occurrence shows a bimodal feature (i.e., peaking in
333 May and October) that is consistent with the temporal distribution of tropical cyclones
334 over the Bay of Bengal. These moisture corridors form over the bay, extend
335 northeastwards, and penetrate inland into Burma, Bangladesh and India. The
336 spatiotemporal characteristics of ARs demonstrate that the southwesterly moisture

transport brings abundant water vapor from the tropics to the northern continent and indicate that tropical cyclones may enhance this poleward moisture transport. Moreover, the high occurrence frequency of ARs in May is different with tropical cyclones but similar with supercyclones (Li et al. 2012), implying that the intensity of tropical cyclones might influence the occurrence of ARs. The low frequency of ARs in summer could be explained by the lack of cyclones and the weak northward water vapor transport due to topographic blocking.

Furthermore, a high correlation between ARs and ERs is verified. Although the fraction of ERs occurring after ARs is relatively small, a large proportion of ARs lead to ERs. In particular, the moisture conveyed by ARs plays an important role in forming ERs during the dry boreal winter. Besides, local convective systems responsible for most summer ERs explain the low occurrence of ERs induced by ARs in summer. On the other hand, the fraction of ARs leading to ERs indicates the potential of ARs in facilitating the landing of ERs considering the crucial role of mountains in the ER formation. In addition, the duration of ARs has minimal influence on the intensity of ERs.

This study for the first time investigates the spatiotemporal characteristics of ARs in low latitudes and their relationship with ERs. Although both are closely correlated with ERs, the dual-peak pattern in occurrence and strong inland penetration of ARs in low latitudes highlight their distinct features from ARs in mid-latitude. These may help

358 better understand the weather extremes and hydrological cycles in this region. One of
359 the limitations that need to appreciate is the use of a single reanalysis dataset: analysis
360 based on more datasets can help generalize the findings of this study. Additionally, the
361 mechanism behind which tropical activities govern ARs needs further exploration.

Acknowledgement

The study is supported by NSFC under 51679119 and 91647107, and by China Postdoctoral Science Foundation under grant 2015T80093. The ERA-Interim dataset used in this study is provided by ECMWF. The authors thank the three anonymous reviewers for their constructive and insightful comments that significantly improve the quality of this work.

368 **Appendix: ARs identified based on two reference latitudes**

369 In this work, we apply two reference latitudes in AR identification and obtain two
370 different groups of ARs. The two reference latitudes are capable to envelope the
371 variation of grid IVT strength over the continent where ARs land (Figure A1).
372 Furthermore, compared with the global AR dataset of Guan and Waliser (2015),
373 although the total number of identified ARs in our work (the oceanic area of a
374 rectangular region extending diagonally from (76.5°E，0°N) to (99°E，24°N)) during
375 1979-2011 is relatively smaller, more than half of our results overlap with the global
376 dataset. Both results show the high frequency of ARs in warm season and a reduction in
377 July (Figure A2). The disparity in the amount of ARs identified can be attributed to
378 three reasons: 1) exclusion of eastward and westward tracks in the back trajectory
379 algorithm to focus on the water vapor directly from the Bay rather than from the
380 Arabian Sea and the South China Sea across land; 2) a much higher fixed lower limit
381 (i.e. 250 kg m^{-1} s^{-1}) (Rutz et al. 2014); 3) exclusion of invalid ARs using equivalent
382 width and direction thresholds during monsoon season (JJAS).
383
384 In addition, the difference between the 24°N and 27°N AR groups might be due to three
385 possible causes: 1) transport delay, 2) reduction in IVT threshold and 3) geometry
386 thresholds related uncertainty. Geometry filtering acting on AR axis structures with
387 ending points on different reference latitudes is likely to yield different results, even if at
388 the same occurrence time. However, as this impact is difficult to quantify, we do not

include the assessment in this section.

To assess the differences caused by transport delay, we choose an average lag of 5 d through sensitivity analysis, considering the time scale of moisture recycling ranges from 2 d to 10 d over the study region and the fast feedback is observed in the summer (van der Ent and Savenije 2011). Only those ARs in 24°N and 27°N occurring within the average lag (i.e., 5 d) are considered to be successive events, by which 24% of the AR events that identified at 27°N can be categorized as successive ones.

Then, we analyze the impact of IVT threshold reduction on the AR identification. Given the lower IVT threshold at 27°N compared with 24°N, we thus apply the threshold at 27°N to the dataset of 24°N to examine the impact of IVT threshold reduction. Based on the IVT threshold at 27°N, 185 ARs are identified at 24°N, of which 26 events overlap with those identified at 27°N.

The different groups of ARs identified based on the two latitudes have a marginal overlap of 6 events. Besides transport delay and IVT threshold reduction, there are still 37% mismatched events in the AR group based on 27°N, which could be partly attributed to geometry related filtering.

Moreover, apparent differences are found between the identified AR groups based on

410 different reference latitudes (Figure A3): 24°N, 27°N and the complete list (i.e., the AR
411 group consisting results from both 24°N and 27°N). Large fluctuations are observed in
412 the inter-annual AR occurrence frequency. For instance, the annual AR occurrence
413 ranges between zero and fourteen in the complete list, with the year 1988 witnessing the
414 most AR events. Also, it is noteworthy that bursts of AR occurrence are observed in the
415 24°N group during each decade, implying the existence of inherent decadal frequency
416 of ARs in this region. On the contrary, the occurrence fluctuation of 27°N groups is
417 relatively milder in the study period with slightly growing trend.
418

Reference

Bao JW, Michelson SA, Neiman PJ, Ralph FM, Wilczak JM. 2006. Interpretation of enhanced integrated water vapor bands associated with extratropical cyclones: Their formation and connection to tropical moisture. *Monthly Weather Review* **134:** 1063-1080.

Berrisford P, Dee DP, Poli P, Brugge R, Fielding K, Fuentes M, Kållberg PW, Kobayashi S, Uppala S, Simmons A. 2011. The ERA-Interim archive Version 2.0. *ERA Report Series*, ECMWF, 23.

Champion AJ, Allan RP, Lavers DA. 2015. Atmospheric rivers do not explain UK summer extreme rainfall. *Journal of Geophysical Research: Atmospheres* **120:** 6731-6741.

Dacre HF, Clark PA, Martinez-Alvarado O, Stringer MA, Lavers DA. 2015. How do atmospheric rivers form? *Bulletin of the American Meteorological Society* **96:** 1243-1255.

Debbage N, Miller P, Poore S, Morano K, Mote T, Marshall Shepherd J. 2017. A climatology of atmospheric river interactions with the southeastern United States coastline. *International Journal of Climatology*.

Dettinger MD, Ralph FM, Das T, Neiman PJ, Cayan DR. 2011. Atmospheric rivers, floods and the water resources of California. *Water* **3**.

Dee DP, Uppala SM, Simmons AJ, Berrisford P, Poli P, Kobayashi S, Andrae U, Balmaseda MA, Balsamo G, Bauer P, Bechtold P, Beljaars ACM, van de Berg L, Bidlot J, Bormann N, Delsol C, Dragani R, Fuentes M, Geer AJ, Haimberger L, Healy

SB, Hersbach H, Hólm EV, Isaksen L, Kållberg P, Köhler M, Matricardi M, McNally AP, Monge-Sanz BM, Morcrette JJ, Park BK, Peubey C, de Rosnay P, Tavolato C, Thépaut JN and Vitart F. 2011. The ERA-Interim reanalysis: configuration and performance of the data assimilation system. 2011. *Quarterly Journal of the Royal Meteorological Society* **137**: 553–597.

Dong W et al. 2016. Summer rainfall over the southwestern Tibetan Plateau controlled by deep convection over the Indian subcontinent. *Nature Communications* **7**: 10925.

Eiras-Barca J, Brands S, Miguez-Macho G. 2016. Seasonal variations in North Atlantic atmospheric river activity and associations with anomalous precipitation over the Iberian Atlantic Margin. *Journal of Geophysical Research: Atmospheres* **121:** 931-948.

Gadgil S. 2003. The Indian monsoon and its variability. *Annual Review of Earth and Planetary Sciences* **31:** 429-467.

Gimeno L, Nieto R, Vázquez M, Lavers DA. 2014. Atmospheric rivers: a mini-review. *Frontiers in Earth Science* **2**.

Guan B, Waliser DE. 2015. Detection of atmospheric rivers: Evaluation and application of an algorithm for global studies. *Journal of Geophysical Research: Atmospheres* **120:** 12514-12535.

Lavers DA, Villarini G. 2013a. Atmospheric rivers and flooding over the Central United States. *Journal of Climate* **26:** 7829-7836.

Lavers DA, Villarini G. 2013b. The nexus between atmospheric rivers and extreme

precipitation across Europe. *Geophysical Research Letters* **40**: 3259-3264.

Lavers, D. A., G. Villarini, R. P. Allan, E. F. Wood, and A. J. Wade, 2012: The detection of atmospheric rivers in atmospheric reanalyses and their links to British winter floods and the large-scale climatic circulation. *Journal of Geophysical Research: Atmospheres*, **117:** D20106.

Lavers DA, Allan RP, Wood EF, Villarini G, Brayshaw DJ, Wade AJ. 2011. Winter floods in Britain are connected to atmospheric rivers. *Geophysical Research Letters* **38:** L23803.

Li Z, Yu W, Li T, Murty VSN, Tangang F. 2012. Bimodal character of cyclone climatology in the Bay of Bengal modulated by monsoon seasonal cycle. *Journal of Climate* **26:** 1033-1046.

Moore BJ, Neiman PJ, Ralph FM, Barthold FE. 2012. Physical Processes Associated with Heavy Flooding Rainfall in Nashville, Tennessee, and Vicinity during 1–2 May 2010: The Role of an Atmospheric River and Mesoscale Convective Systems. *Monthly Weather Review* **140**: 358–378.

Neiman PJ, Ralph FM, White AB, Kingsmill DE, Persson POG. 2002. The statistical relationship between upslope flow and rainfall in California's coastal mountains: Observations during CALJET. *Monthly Weather Review* **130:** 1468-1492.

Neiman PJ, Ralph FM, Wick GA, Lundquist JD, Dettinger MD. 2008a. Meteorological characteristics and overland precipitation impacts of atmospheric rivers affecting the west coast of North America based on eight years of SSM/I satellite observations. *Journal of Hydrometeorology* **9:** 22-47.

485 Neiman PJ, Ralph FM, Wick GA, Kuo YH, Wee TK, Ma Z, Taylor GH, Dettinger MD.
486 2008b. Diagnosis of an Intense Atmospheric River Impacting the Pacific Northwest:
487 Storm Summary and Offshore Vertical Structure Observed with COSMIC Satellite
488 Retrievals. *Monthly Weather Review* **136**: 4398-4420.
489 Ralph FM, Neiman PJ, Wick GA. 2004. Satellite and CALJET aircraft observations of
490 atmospheric rivers over the Eastern North Pacific Ocean during the winter of 1997/98.
491 *Monthly Weather Review* **132:** 1721-1745.
492 Ralph FM, Neiman PJ, Rotunno R. 2005. Dropsonde observations in low-level jets
493 over the Northeastern Pacific Ocean from CALJET-1998 and PACJET-2001: Mean
494 vertical-profile and atmospheric-river characteristics. *Monthly Weather Review* **133:**
495 889-910.
496 Ralph FM, Neiman PJ, Wick GA, Gutman SI, Dettinger MD, Cayan DR, White AB.
497 2006. Flooding on California's Russian River: Role of atmospheric rivers.
498 *Geophysical Research Letters* **33,** L13801.
499 Ralph FM, Dettinger MD. 2011a. Storms, floods, and the science of atmospheric
500 rivers. *Eos, Transactions American Geophysical Union* **92:** 265-266.
501 Ralph FM, Neiman PJ, Kiladis GN, Weickmann K, Reynolds DW. 2011b. A
502 Multiscale Observational Case Study of a Pacific Atmospheric River Exhibiting
503 Tropical–Extratropical Connections and a Mesoscale Frontal Wave. *Monthly Weather*
504 *Review* **139**: 1169-1189.
505 Rutz JJ, Steenburgh WJ, Ralph FM. 2014. Climatological characteristics of
506 atmospheric rivers and their inland penetration over the Western United States.

Monthly Weather Review **142:** 905-921.

Schneider T, Bischoff T, Haug GH. 2014. Migrations and dynamics of the intertropical convergence zone. *Nature* **513**: 45-53.

Stohl A, Forster C, Sodemann H. 2008. Remote sources of water vapor forming precipitation on the Norwegian west coast at 60°N–a tale of hurricanes and an atmospheric river. *Journal of Geophysical Research: Atmospheres* **113:** D05102.

van der Ent RJ, Savenije HHG. 2011. Length and time scales of atmospheric moisture recycling. *Atmosphric Chemistry and Physics* **11:** 1853-1863.

Viale M, Nuñez MN. 2010. Climatology of winter orographic precipitation over the subtropical central Andes and associated synoptic and regional characteristics. *Journal of Hydrometeorology* **12:** 481-507.

Wu S, Pan T, Cao J, He D, Xiao Z. 2012. Barrier-corridor effect of longitudinal range-gorge terrain on monsoons in Southwest China. *Geographical Research* **1**: 1-13.

Zhao T, Zhao J, Hu H, Ni G. 2015. Source of atmospheric moisture and precipitation over China's major river basins. *Frontiers of Earth Science* **10:** 159-170.

Zhu Y, Newell RE. 1998. A proposed algorithm for moisture fluxes from atmospheric rivers. *Monthly Weather Review* **126:** 725-735.

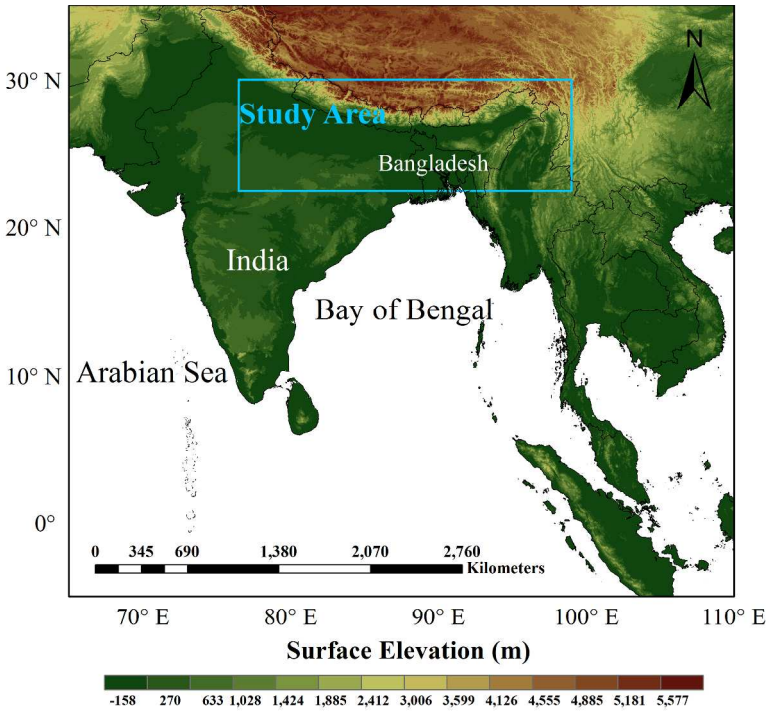

Figure 1 Observed (30 arc s) topography (shaded in m) for the Bay of Bengal (BOB) and part of Asia. The location of study area is shown in blue box (from (76.5°E, 22.5°N) to (99°E, 30°N)). The west-east boundary is based on the extent of BOB and the south-north boundary represents the northern continental area between coast and the Himalayas. The country boundaries are represented by black lines.

297x210mm (300 x 300 DPI)

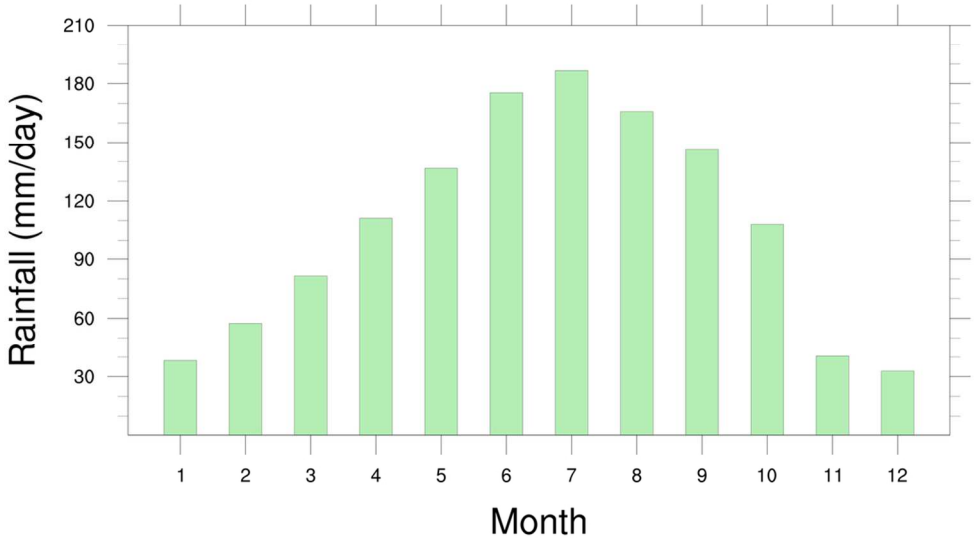

Figure 2 Monthly extreme rainfall thresholds defined as the 90th percentile of the maximum daily rainfall (larger than 1 mm) over the study region during 1979-2011.

105x105mm (300 x 300 DPI)

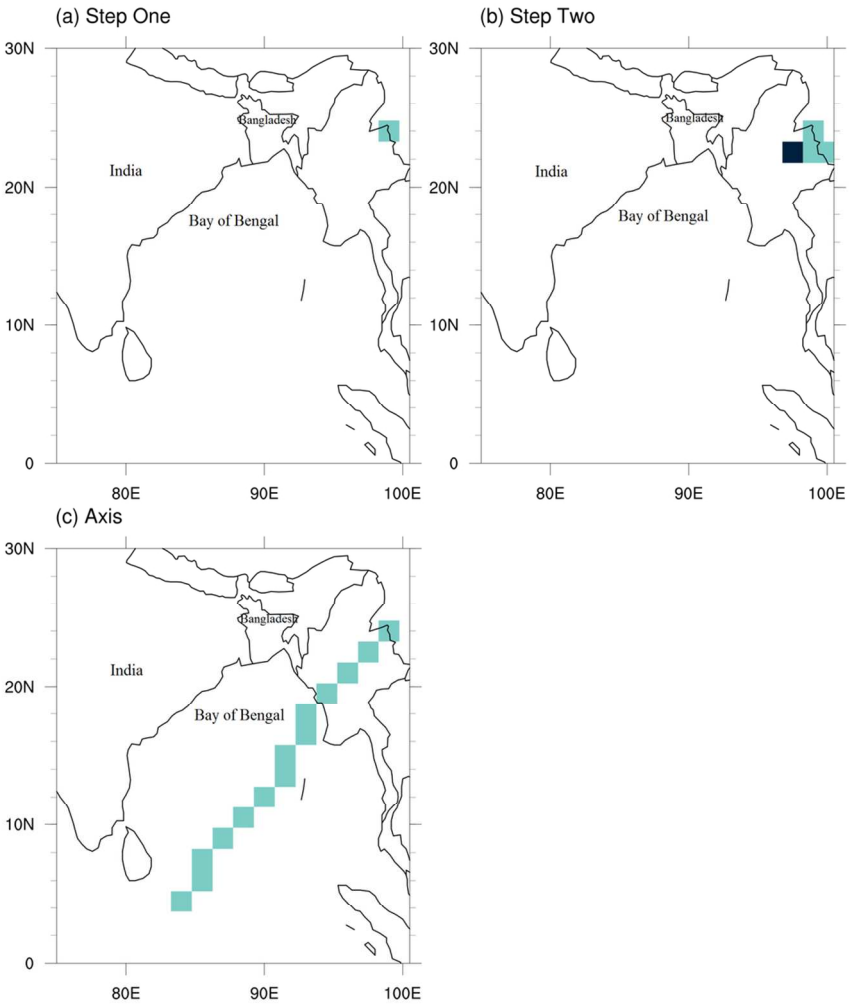

Figure 3 The AR axis structure identification algorithm. (a) The blue grid indicates the location of maximum IVT between 76.5°E and 99°E at 24°N (reference latitude), which serves as the ending point of the axis. (b) The next step is to search the adjacent grid cells (to the south/ southeast/ southwest) for highest IVT. The black grid represents the selected highest IVT location. (c) Repeat step two for 13 times and obtain the axis structure (the connected blue line).

105x105mm (300 x 300 DPI)

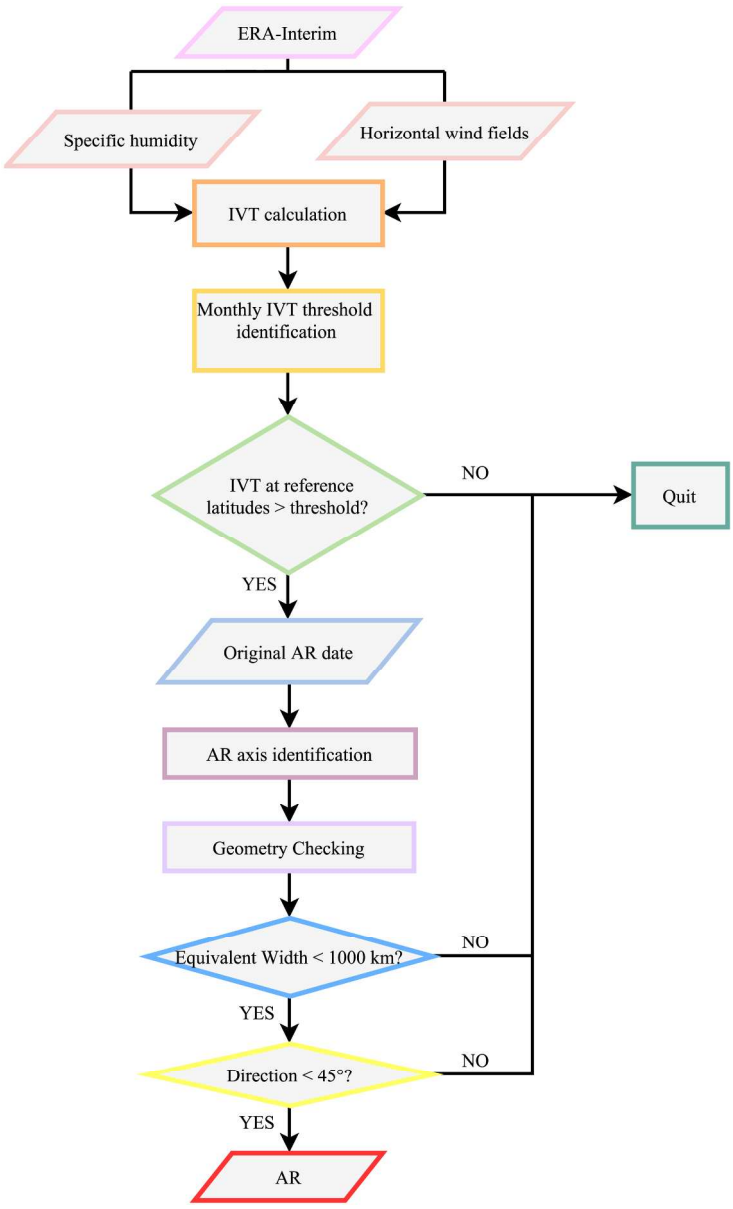

Figure 4 The brief framework for AR identification algorithm.

164x270mm (300 x 300 DPI)

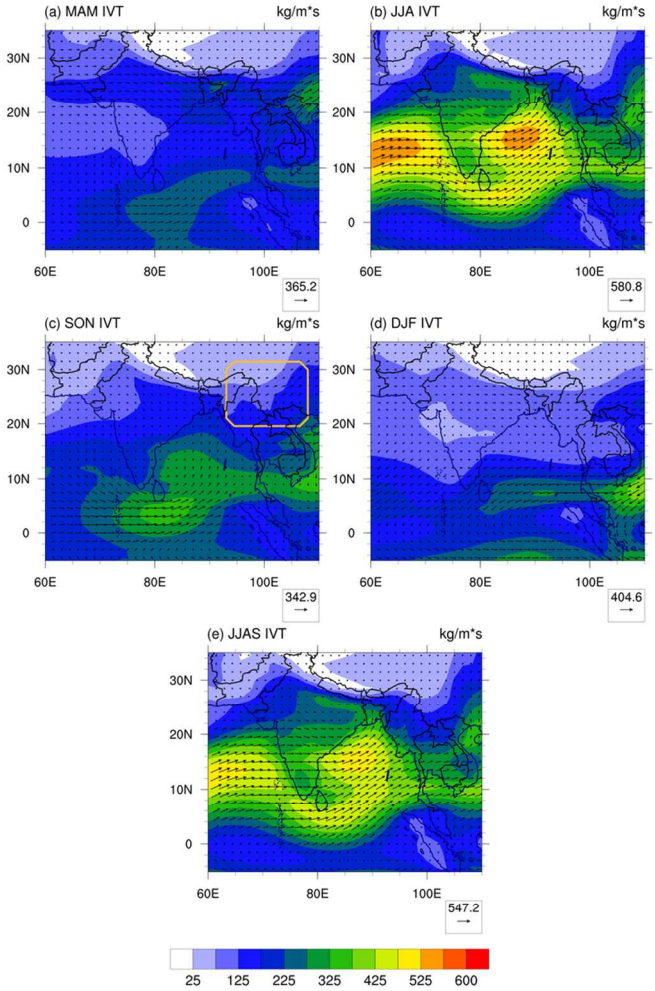

Figure 5 The seasonal mean IVT (in $kg/m^{-1}s^{-1}$) in (a) spring, (b) summer, (c) autumn, (d) winter and (e) monsoon season. The yellow box (from (21°N, 95°E) to (30° N, 106°E)) represents the spatial scope of Longitudinal Range-Gorge Region (Wu et al. 2012).

105x105mm (300 x 300 DPI)

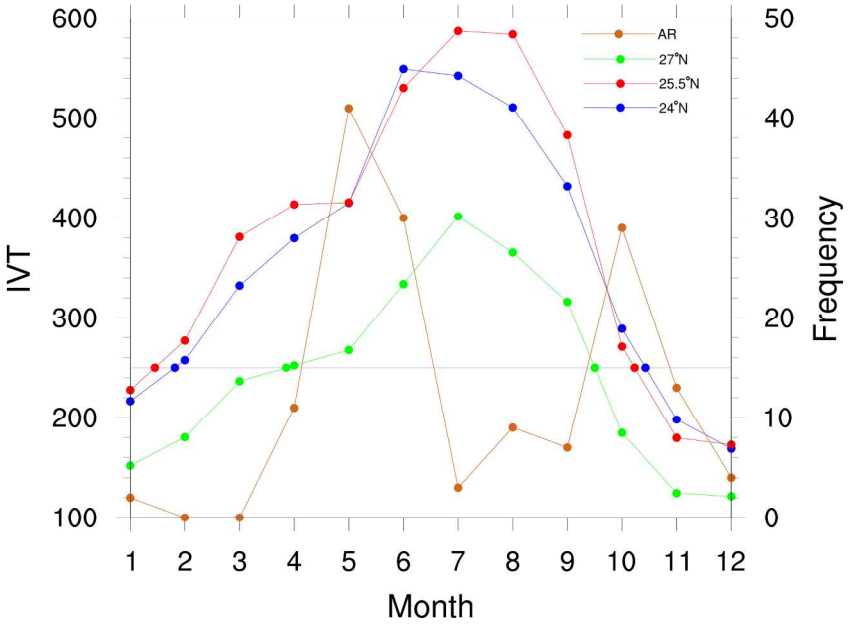

Figure 6 The monthly IVT strength thresholds at 24°N (blue), 25.5°N (red) and 27°N (green) in the study area (left axis). The IVT strength threshold is determined as follows. The maximum values of IVT at certain latitudes at 1200 UTC of each day are first regrouped by month, then the 85th percentiles of each group are determined as the monthly thresholds. The purple line of 250 kg m^{-1} s^{-1} represents the lower limit of IVT strength (left axis). The chocolate line displays the intra-annual distribution of ARs identified over the Bay of Bengal during 1979-2011(right axis).

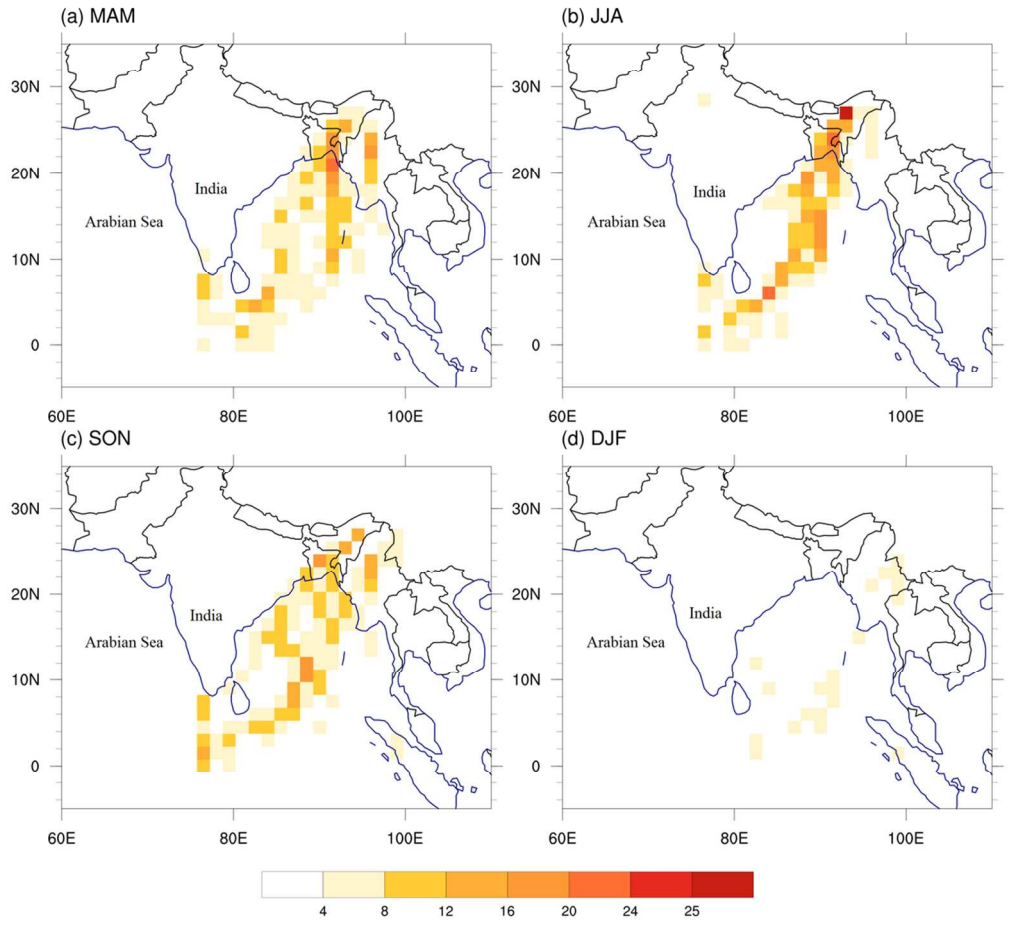

Figure 7 The spatial occurrence of ARs that is shown as the seasonal-accumulative occurrence frequency of AR axis in each grid.

105x105mm (300 x 300 DPI)

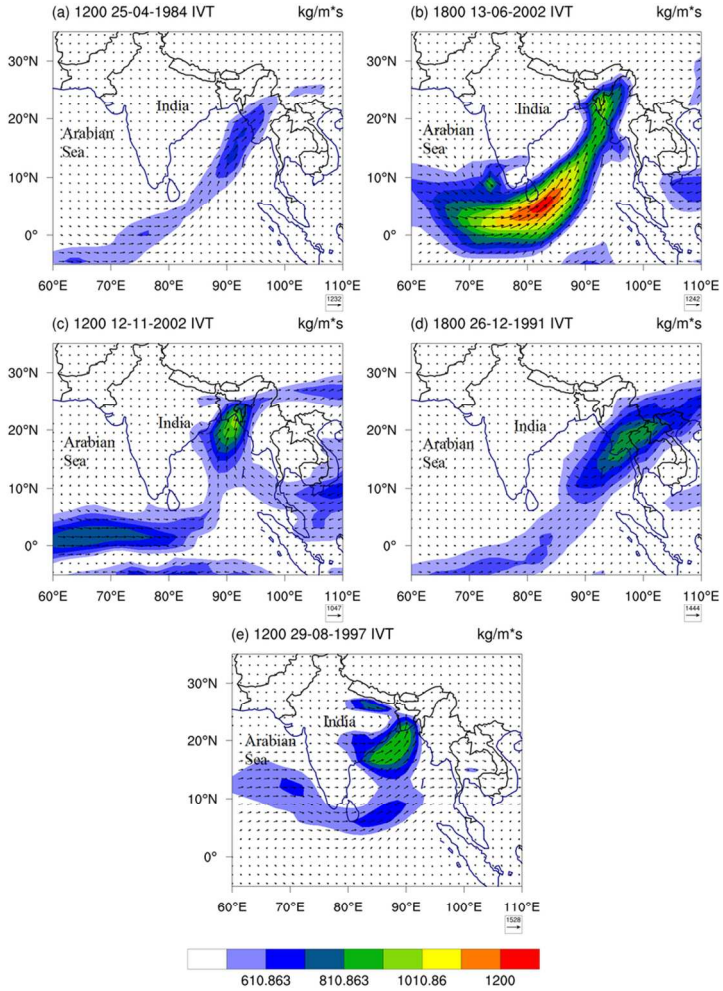

Figure 8 Examples of five ARs shown in IVT (in kg $m^{-1}s^{-1}$) at (a) 1200UTC 25th April 1984, (b) 1800UTC 13th June 2002, (c) 1200UTC 12th November 2002, (d) 1800UTC 26th December 1991, and (e) 1200 UTC 29th August 1997. Note that the lower limit is the IVT threshold of the corresponding month.

105x105mm (300 x 300 DPI)

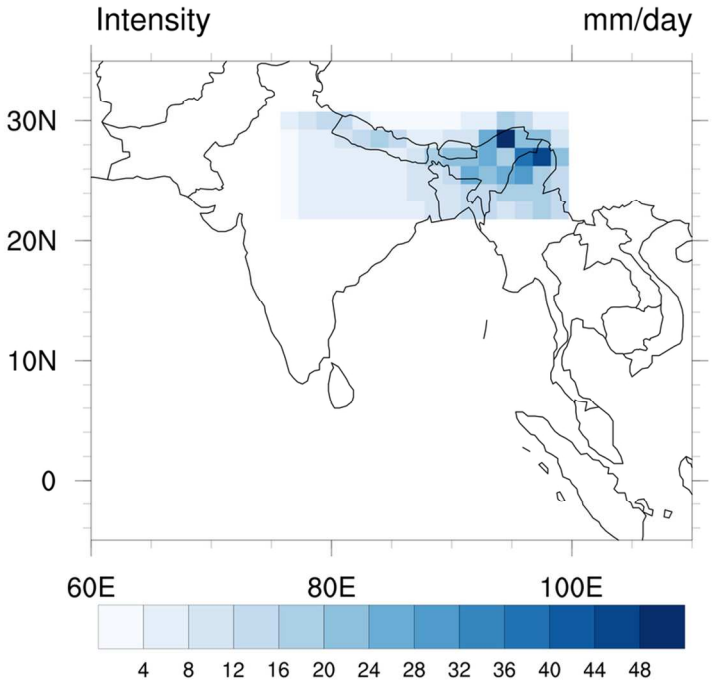

Figure 9 the spatial distribution of mean ER intensity over study area.

105x105mm (300 x 300 DPI)

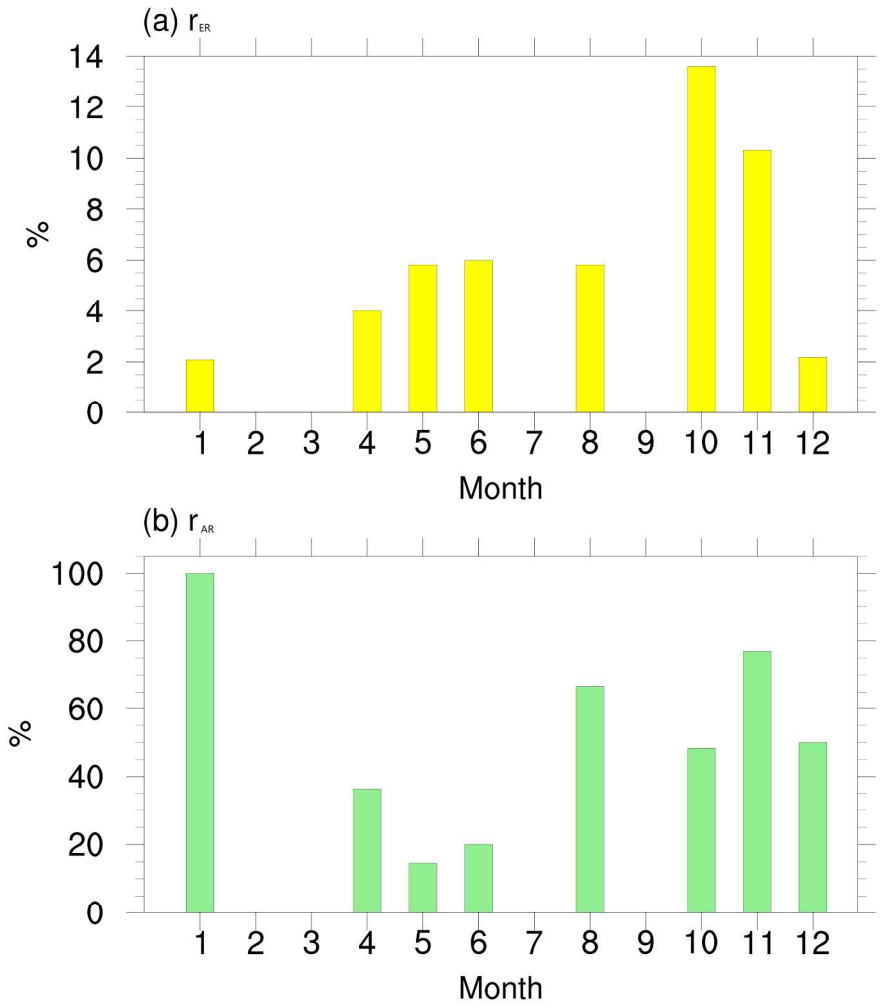

Figure 10 (a) and (b) are r_{ER} (the occurrences of AREs over all ERs) and r_{AR}(the occurrences of AERs over all ARs) respectively.

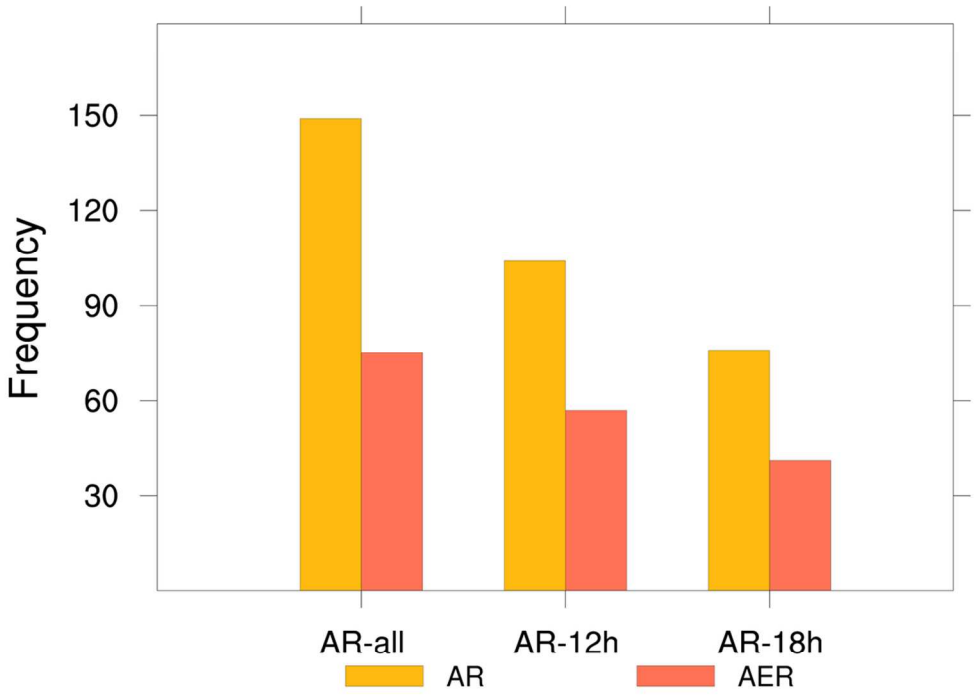

Figure 11 Frequency of AERs in three groups.

105x105mm (300 x 300 DPI)

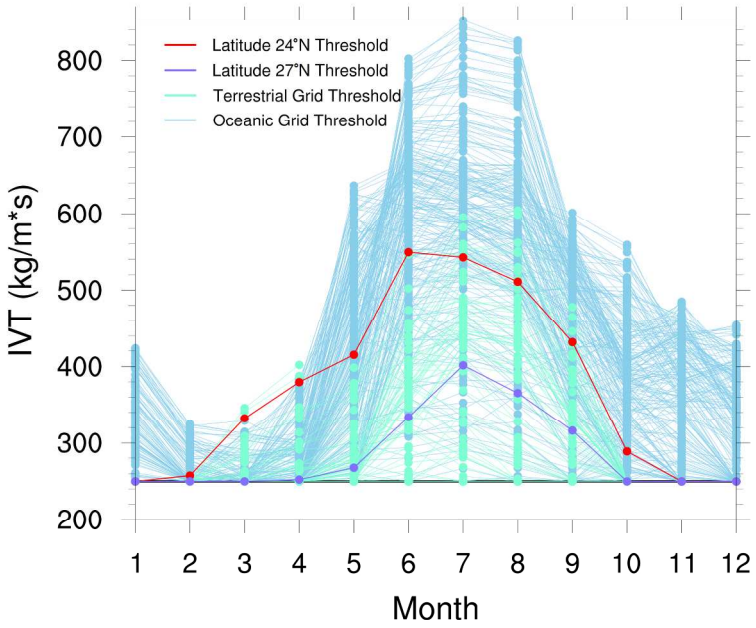

Figure A1 Monthly variations of IVT strength threshold of different areas: oceanic grids (blue, from (76.5°E, 0°N) to (99°E, 22.5°N)), terrestrial grids (green, from (76.5°E, 24°N) to (99°E, 30°N)), reference latitude 24°N (red), and reference latitude 27°N (purple). The black line indicates the lower limit of IVT threshold of 250 kg m^{-1} s^{-1}.

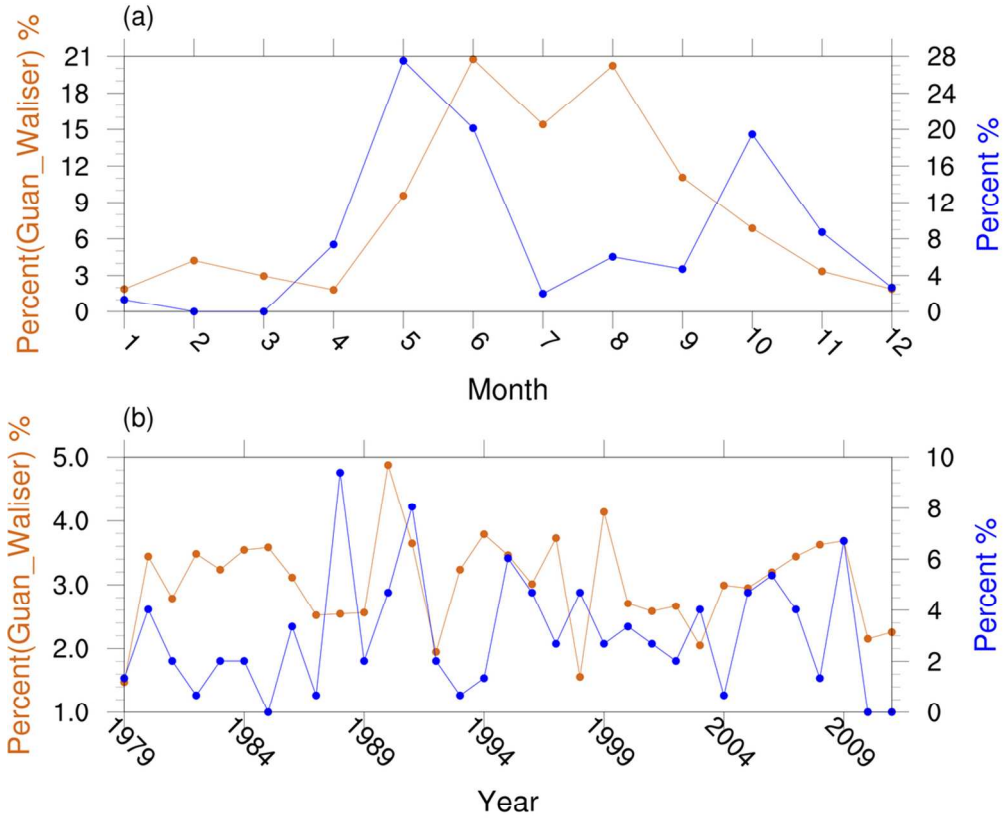

Figure A2 The (a) intra-annual and (b) inter-annual AR distribution of Guan and Waliser global AR dataset (brown) and our results (blue).

105x105mm (300 x 300 DPI)

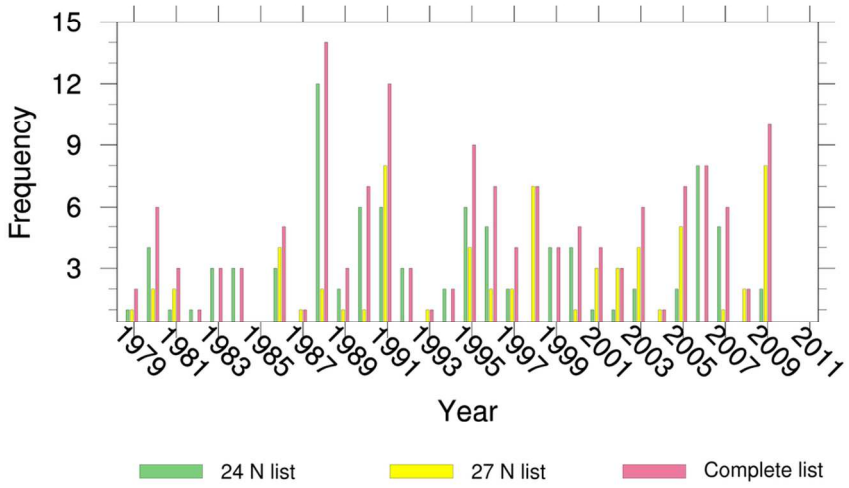

Figure A3 Time series of identified ARs over 1979-2011. The green bars and yellow bars show the 24°N and 27°N list respectively, and the pink bars represents the complete list.

105x105mm (300 x 300 DPI)

Figure Captions:

Figure 1 Observed (30 arc s) topography (shaded in m) for the Bay of Bengal (BOB) and part of Asia. The location of study area is shown in blue box (from (76.5°E，22.5°N) to (99°E，30°N)). The west-east boundary is based on the extent of BOB and the south-north boundary represents the northern continental area between coast and the Himalayas. The country boundaries are presented by black lines.

Figure 2 Monthly extreme rainfall thresholds defined as the 90th percentile of the maximum daily rainfall (larger than 1 mm) over the study region during 1979-2011.

Figure 3 The AR axis structure identification algorithm. (a) The blue grid indicates the location of maximum IVT between 76.5°E and 99°E at 24°N (reference latitude), which serves as the ending point of the axis. (b) The next step is to search the adjacent grid cells (to the south/ southeast/ southwest) for highest IVT. The black grid represents the selected highest IVT location. (c) Repeat step two for 13 times and obtain the axis structure (the connected blue line).

Figure 4 The flowchart for AR identification algorithm.

Figure 5 The seasonal mean IVT (in kg/m^{-1}s^{-1}) in (a) spring, (b) summer, (c) autumn, (d) winter and (e) monsoon season. The yellow box (from (21°N, 95°E) to (30° N, 106°E)) represents the spatial scope of Longitudinal Range-Gorge Region (Wu et al. 2012).

Figure 6 The monthly IVT strength thresholds at 24°N (blue), 25.5°N (red) and 27°N (green) in the study area (left axis). The IVT strength threshold is determined as follows. The maximum values of IVT at certain latitudes at 1200 UTC of each day are first regrouped by month, then the 85th percentiles of each group are determined as the monthly thresholds. The purple line of 250 kg m^{-1} s^{-1} represents the lower limit of IVT strength (left axis). The chocolate line displays the intra-annual distribution of ARs identified over the Bay of Bengal during 1979-2011(right axis).

Figure 7 The spatial occurrence of ARs that is shown as the seasonal-accumulative occurrence frequency of AR axis in each grid.

Figure 8 Examples of five ARs shown in IVT (in kg m^{-1}s^{-1}) at (a) 1200UTC 25th April 1984, (b) 1800UTC 13th June 2002, (c) 1200UTC 12th November 2002, (d) 1800UTC 26th December 1991, and (e) 1200 UTC 29th August 1997. Note that the lower limit is the IVT threshold of the corresponding month.

Figure 9 the spatial distribution of mean ER intensity over study area.

Figure 10 (a) and (b) are r_{ER} (the occurrences of AREs over all ERs) and r_{AR} (the

occurrences of AERs over all ARs) respectively.

Figure 11 Frequency of AERs in three groups.

Figure A1 Monthly variations of IVT strength threshold of different areas: oceanic grids (blue, from (76.5°E, 0°N) to (99°E, 22.5°N)), terrestrial grids (green, from (76.5°E, 24°N) to (99°E, 30°N)), reference latitude 24°N (red), and reference latitude 27°N (purple). The black line indicates the lower limit of IVT threshold of 250 kg m^{-1} s^{-1}.

Figure A2 The (a) intra-annual and (b) inter-annual AR distribution of Guan and Waliser (2015) global AR dataset (brown) and our results (blue).

Figure A3 Time series of identified ARs over 1979-2011. The green bars and yellow bars show the 24°N and 27°N list respectively, and the pink bars represents the complete list.